JOURNAL OF SOLID STATE CHEMISTRY **141,** 537–545 (1998)
ARTICLE NO. SC988016

Crystal Structure and Phase Transition in the Defect Pyrochlore NH_4NbWO_6

C. A. Perottoni,* J. Haines,† and J. A. H. da Jornada*,[1]

*Instituto de Física, UFRGS, 91501-970 Porto Alegre, Brazil; and †Laboratoire de Physico-Chimie des Matériaux, CNRS, 1 Place A. Briand, 92190 Meudon, France

Received October 27, 1997; in revised form August 25, 1998; accepted August 31, 1998

The crystal structure of ammonium tungstoniobate is revised as some features observed in its X-ray diffraction pattern are not consistent with the extinction conditions of space group $Fd\bar{3}m$, commonly assigned to this compound. A better agreement between the observed and calculated X-ray powder diffraction patterns was obtained by performing a Rietveld refinement with a structural model using the noncentrosymmetric space group $F\bar{4}3m$. The temperature dependence of the $Fd\bar{3}m$-forbidden 420 Bragg peak intensity indicates a continuous transition at 455 K from the space group $F\bar{4}3m$ to a more symmetrical, high-temperature phase, with space group $Fd\bar{3}m$.

INTRODUCTION

Pyrochlore compounds of general stoichiometry $A_2B_2X_6X'$ have been investigated since the early work on pyrochlorite, $CaNaNb_2O_6F$, about 60 years ago (1). This class of compounds exhibits many interesting physical properties such as ferroelectricity and fast ionic conductivity (2–4), which make some of them suitable choices for applications in fuel cells and other similar devices. Among them, several defect pyrochlores AB_2O_6 (5) (where A is, e.g., H, NH_4, Rb, Cs, Cd, K, Na, or Tl and B is a small cation, e.g., Nb, W, Ta, Te, Sb, or V) have been studied by many different experimental techniques, including X-ray and neutron diffraction, inelastic neutron scattering, Raman and infrared spectroscopy, thermal analysis, impedance spectroscopy, NMR, and second-harmonic generation, leading in some cases to a successful understanding of their physical properties in terms of particular features of their crystal structures (see, e.g., (6–17)).

One of the earliest works on the defect pyrochlore NH_4NbWO_6, by Groult, Michel, and Raveau, involved the study of its thermal behavior by thermal gravimetry and differential thermal analysis (18). Although the existence of ionic conductivity in AB_2O_6 compounds already was known in the early 1970s, the interest in NH_4NbWO_6 was just renewed about 10 years ago when Brunner and Tomandl produced pellets of NH_4NbWO_6 with the goal of obtaining a feasible proton conductor (19). Since then, this compound has been studied by neutron diffraction (20), NMR (21), and impedance spectroscopy at pressures up to 3 GPa and temperatures between 295 and 473 K (22). Recently, an interesting phenomenon of pressure-induced water insertion from the pressure medium was shown to occur with this compound, leading to an unexpected increase of the unit cell volume under high pressure (23).

The crystal structure of the ammonium tungstoniobate pyrochlore is usually described as a rigid framework of corner-sharing $(Nb,W)O_6$ octahedra with a network of ammonium ions loosely bound to the rest of the structure and responsible for the ionic conduction (19). The crystal symmetry of this compound is commonly assigned to the space group $Fd\bar{3}m$ (No. 227), with $Z = 8$ (20, 21) and only one free positional parameter associated with the site occupied by the oxygen atoms. However, as will be shown, this assigned space group does not account for a weak peak observed in the X-ray powder diffraction pattern at ambient conditions and also does not reproduce the intensities of some other weak peaks in the diffraction pattern.

In this paper we present a detailed study of the defect pyrochlore NH_4NbWO_6 crystal structure, based on the Rietveld refinement of its X-ray powder diffraction pattern obtained under ambient conditions, as well as the temperature dependence of one $Fd\bar{3}m$-forbidden reflection.

EXPERIMENTAL

The powder samples of NH_4NbWO_6 and $RbNbWO_6$ were prepared at the Institut für Werstoffwissenschaften, Universität Erlangen-Nurnberg. NH_4NbWO_6 was prepared by ion exchange of $RbNbWO_6$ in molten NH_4NO_3, following the procedure described in detail by Brunner (19).

[1] To whom correspondence should be addressed. E-mail: perott@if.ufrgs.br.

0022-4596/98 $25.00

Electron microprobe analysis of NH_4NbWO_6 gives an upper limit of about 1.4% in mass of rubidium after ion exchange. When a sample of NH_4NbWO_6 was heated above 950 K, thermal gravimetric analysis (TGA) yielded a weight loss of 6.28%. From the thermal decomposition equation (according to Ref. (18))

$$NH_4NbWO_6 \xrightarrow{\Delta} NbWO_{5.5} + NH_3 + \tfrac{1}{2}H_2O \qquad [1]$$

the expected value of the weight loss for a full stoichiometric amount of ammonium in NH_4NbWO_6 is 6.60%. The difference from the actual value is in accordance with the residual amount of rubidium in the form of $RbNbWO_6$ not exchanged and $RbCO_3$, also identified in the diffraction pattern as a minor impurity. Both compounds were taken into account in the Rietveld refinement as second and third phases.

The X-ray powder diffraction data were obtained using Cu$K\alpha$ radiation from a sealed tube operating at 35 kV and 10 mA on a Siemens D500 diffractometer. The experimental setup consisted of Soller slits in the incident beam, two 1° divergence slits, 1° receiving and 0.15° scatter slits, and a graphite monochromator in the diffracted beam. Rietveld refinement of the room temperature powder pattern was performed with the program Fullprof (24). Special care was taken to reduce peak asymmetry due to axial divergence, including the use of receiving and scatter slits with the length reduced to 4 mm. A pseudo-Voigt function convoluted with an axial divergence asymmetry function was used to model the peak profile (25, 26). Peak intensities were corrected for the presence of the graphite monochromator in the secondary beam, and the peak profile was calculated within ± 15 FWHM (full width at half maximum) from the peak position.

Low- and high-temperature X-ray diffraction patterns were obtained in an evacuated sample holder refrigerated with liquid nitrogen and controlled by a resistive heater. The temperature was kept constant within ± 0.1 K. Step-scan data were collected over the angular range between 36° and 40° (2θ Cu$K\alpha$), with a step size of 0.02° and 4s integration time, from 94 to 533 K (above this temperature the compound begins to decompose). At the upper temperature limit, data were collected with an integration time of 20 s per step. The dependence on temperature of the integrated intensity of the adjacent 331 and 420 reflections was followed by fitting them to a pair of pseudo-Voigt functions. In addition, a complete scan from 10° to 140° (2θ Cu$K\alpha$) was performed at each temperature to observe eventual modifications in the whole diffraction pattern. In the temperature range from 100 to 300 K, step-scan data were corrected for sample displacement using a nickel powder internal standard to follow the variation with temperature of the ammonium tungstoniobate lattice parameter. An additional X-ray diffraction pattern of LaB_6 standard reference material (NIST SRM660 (27)) was carried out to compare the FWHM angular dependency in the X-ray diffraction patterns of NH_4NbWO_6 and $RbNbWO_6$ and the intrinsic instrumental linewidth.

Infrared transmission spectra of ammonium tungstoniobate samples dispersed in KBr disks were obtained with a Bomem FTIR Model MB100, equipped with a DTGS detector and KBr beamsplitter, in the spectral range from 350 to 4000 cm^{-1}. A specially designed vacuum cell with sodium chloride windows was used to study the process of high-temperature water loss from the sample of NH_4NbWO_6 dispersed in KBr (28).

RESULTS AND DISCUSSION

The experimental room temperature X-ray diffraction pattern of NH_4NbWO_6 is shown in Fig. 1, together with the profile calculated with a structural model based on the space group $Fd\bar{3}m$. The lattice parameter as well as profile parameters were refined, but atomic positions and anisotropic displacement parameters were kept fixed to the values given by Kuntz (20). All diffraction peaks of NH_4NbWO_6 have a FWHM slightly greater than their corresponding values in $RbNbWO_6$, but no clear departure from cubic symmetry was observed.

According to Fig. 1, there is a good general agreement between calculated and experimental patterns over the whole angular range. However, as can be seen in the expanded view (Fig. 1b), there is an unexpected weak peak at 38.8 ° (2θ Cu$K\alpha$) that could be indexed as the 420 reflection of a face-centered cubic lattice with the same lattice parameter, thereby violating the $Fd\bar{3}m$ reflection condition $hk0$: $h + k = 4n$. The integrated intensity of this peak, as well as those of the 220, 442, and 644 Bragg peaks among others, decreases noticeably when the temperature is raised, as shown in Fig. 2. It should be noted that although the 442 and 644 peaks are permitted by the general reflection conditions of space group $Fd\bar{3}m$, they are forbidden by this particular structure, because they simultaneously violate the reflection conditions associated with the metal, nitrogen, and oxygen sites.

The intensity decrease with temperature of Bragg peak 420, as can be seen in Fig. 3, is continuous over the temperature range between 250 and 533 K and approaches zero at high temperatures. This behavior is entirely reversible and no hysteresis could be detected. Above 250 K, differential scanning calorimetry (DSC) results for NH_4NbWO_6 showed no thermal event that could be associated with a first-order transition, in accordance with the early results of Groult, Michel, and Raveau (18). These results are consistent with a continuous, second-order phase transition from the stable form under ambient conditions to a more symmetrical, high-temperature phase. This conclusion imposes some restrictions on the space group of the ambient

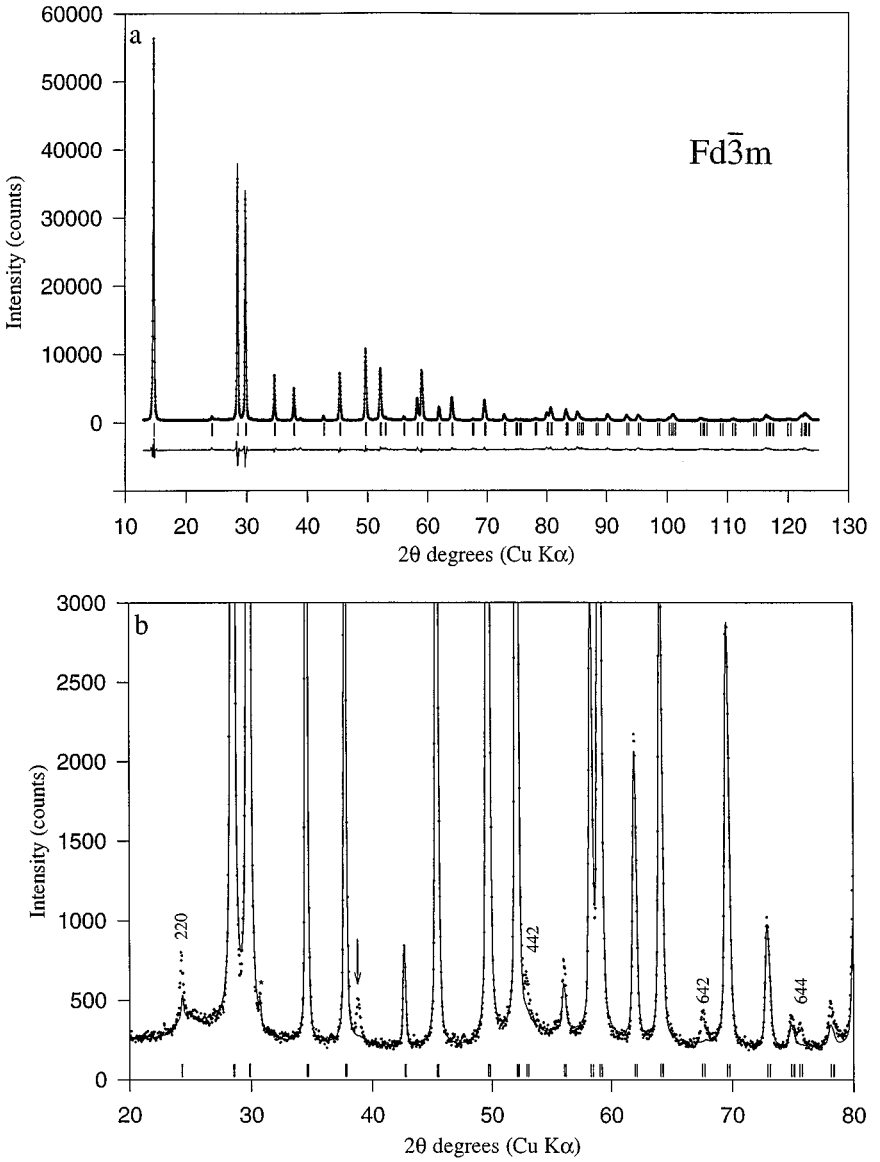

FIG. 1. (a) X-ray powder diffraction pattern of NH_4NbWO_6 under ambient conditions. Dots indicate the raw data points and the solid line is the refined profile using the space group $Fd\bar{3}m$. Plotted on the same scale below is the difference between the observed and calculated profiles. The tick marks indicate the calculated positions of all permitted reflections in $Fd\bar{3}m$. (b) Expanded view of (a), with labels in some relevant peaks that are not well accounted for using this structural model. The asterisk marks the most intense peak of $RbCO_3$. The arrow indicates the Bragg peak 420 that violates the $Fd\bar{3}m$ reflection condition ($hk0$): $h + k = 4n$.

temperature phase, which should be a subgroup of $Fd\bar{3}m$ (the space group of the high-temperature phase), according to Landau theory of second-order phase transitions (29).

Following Kovalev (30), there are only four cubic subgroups of space group $Fd\bar{3}m$. Of these, only two can account for the weak 420 peak observed in the X-ray diffraction pattern at ambient temperature, namely the space groups $F\bar{4}3m$ and $F23$. The latter is a subgroup of the former and thus, to avoid using an unnecessarily low-symmetry space group, we choose the space group $F\bar{4}3m$ to perform a Rietveld refinement of the room temperature X-ray diffraction pattern of ammonium tungstoniobate. This choice is also consistent with Landau and Lifshitz's conditions for a second-order phase transition. Indeed, factor group analysis of the ammonium tungstoniobate structure indicates that the active irreducible representation A_{2u} that drives the transition from $Fd\bar{3}m$ to $F\bar{4}3m$ is present among the irreducible representations of the high-symmetry phase (31).

The temperature dependence of the integrated intensity of the Bragg peak 420 (Fig. 3) can be well reproduced, even far

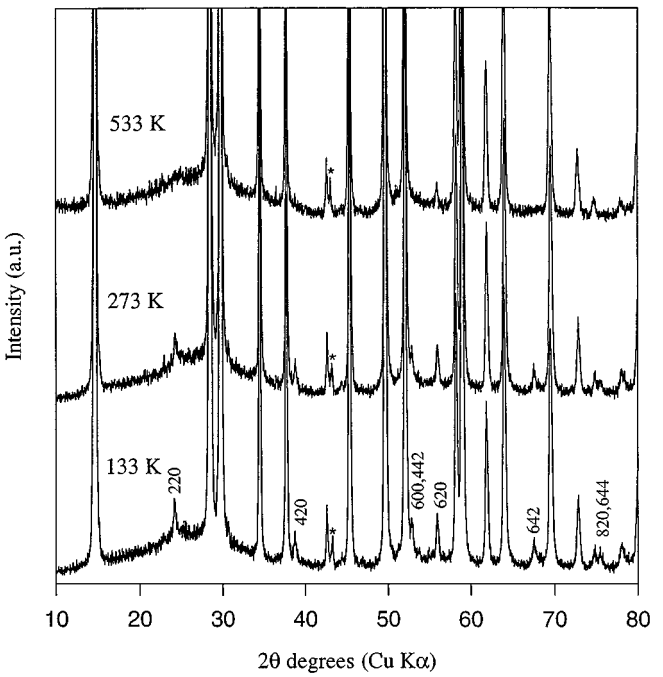

FIG. 2. Thermal evolution of the NH_4NbWO_6 X-ray powder diffraction pattern, indicating the gradual disappearance of labeled peaks. The asterisk marks a peak from the sample holder.

below the transition temperature, by fitting to the usual power law dependence (32)

$$I \propto \left(1 - \frac{T}{T_c}\right)^{\chi} \qquad [2]$$

yielding a critical temperature (T_c) of 455 ± 11 K for the $F\bar{4}3m$ to $Fd\bar{3}m$ transition, with the best fitted value of χ being 0.68 ± 0.1. However, as already observed in experiments done with $RbNbWO_6$, it is likely that T_c can be dependent to some extent on the given sample, due to the presence of impurities, especially residual tightly bound water in the sample, as was previously reported for other defect pyrochlores (33, 34). Some impurities may also account for the residual intensity of the 420 peak left above the critical temperature.

The slight discontinuity observed in Fig. 3 at about 220 K also appears in the temperature dependence of the NH_4NbWO_6 lattice parameter (Fig. 4) and in low-temperature DSC measurements and is probably associated with a weak first-order transition. There is some evidence that this low-temperature transition could be the same as the displacive high-pressure phase transition observed in this compound at 4 GPa, whose only visible effect is an increase of NH_4NbWO_6 compressibility above the transition pressure (36).

Infrared transmission spectroscopy of the ammonium pyrochlore, dispersed in KBr that had been dried overnight immediately before the measurements, indicates a water content below the limit of detectability by conventional thermogravimetric methods. The resulting infrared transmittance spectrum can be seen in Fig. 5, where the O–H stretching band at 3530 cm^{-1} is clearly distinguishable. This result is consistent with the well-known fact that some defect pyrochlores AB_2O_6 are hygroscopic, depending on the nature of the large cation A (33–35). This water was irreversibly driven out by heating the sample in a specially designed vacuum cell at 520 K for 1 h, as could be inferred by the almost complete disappearance of the O–H stretching band after thermal treatment. Therefore, since the high-temperature X-ray diffraction patterns were also taken under vacuum, the reversibility observed in the temperature dependence of the 420 peak intensity implies that the trace water content in the ammonium pyrochlore has no special role in the phase transition from $Fd\bar{3}m$ to $F\bar{4}3m$.

The good agreement between the pattern calculated using space group $F\bar{4}3m$ and the experimental X-ray powder diffraction pattern can be seen in Fig. 6. Details about the Rietveld analysis of NH_4NbWO_6 using a model based on the $F\bar{4}3m$ space group are summarized in Table 1. The resulting atomic positions and atomic displacement parameters are given in Table 2. The hydrogen atoms from the ammonium ions were not taken into account in the structural model because of their intrinsically low atomic X-ray scattering factor. The atomic position and anisotropic atomic displacement parameters for Nb^{5+} and W^{6+} ions were constrained to be equal during the refinement. The resulting oxygen positions at 24g $(x, 1/4, 1/4)$ and 24f $(x, 0, 0)$—$F\bar{4}3m$—are in good agreement with a point of minimum energy in the electrostatic potential surface calculated for this structure according to the method of Bertaut (37, 38). The resulting crystal structure of NH_4NbWO_6 is depicted in Fig. 7.

An improvement in the agreement between the calculated and the experimental powder pattern was obtained by relaxing the restraints imposed on the position of the nitrogen ions. In this case, the refinement converges in such a way that the nitrogen ions are slightly displaced from the special positions 4b $(1/2, 1/2, 1/2)$ and 4d $(3/4, 3/4, 3/4)$, resulting in two partially filled 16e (x, x, x) sites with $x = 0.511(2)$ and $x = 0.797(2)$, respectively. Because of the high correlation between the nitrogen free position parameters and its isotropic displacement factor, they were refined separately, in an attempt to avoid unphysical results. Even so, the final values can be biased, especially considering the difficulty in modeling light-atom positions from X-ray diffraction data. Accordingly, the small nitrogen atomic displacement parameter reported in Table 2 probably results from the statistical distribution of the ammonium ions among several equivalent positions in the two

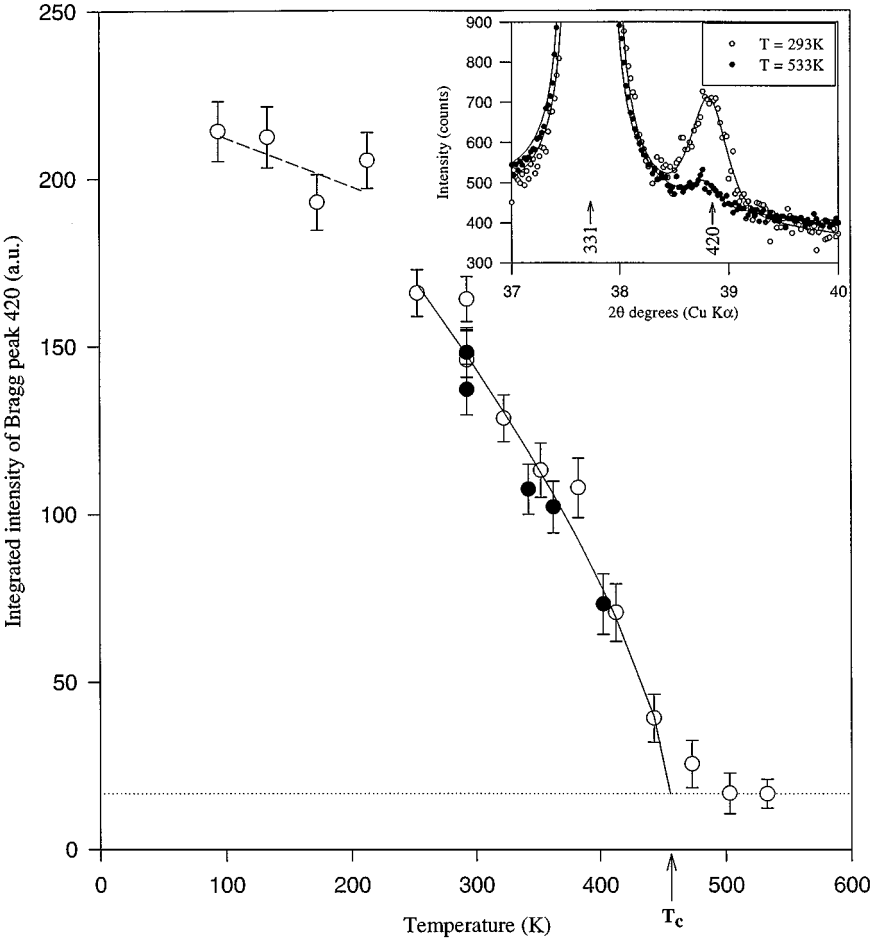

FIG. 3. Temperature dependence of the integrated intensity of the NH_4NbWO_6 420 reflection. Extrapolation of the data indicates the transition temperature (T_c) from the noncentrosymmetric $F\bar{4}3m$ to the centrosymmetric $Fd\bar{3}m$ high-temperature phase. Filled circles indicate results obtained in the reverse cycle in which the sample previously heated to 530 K was cooled while maintained under vacuum. The solid line is the resulting fitting to Eq. [2]. The inset at the top right corner shows an expanded view of the ammonium tungstoniobate X-ray diffraction pattern, illustrating the quality of the fitting procedure and the 420 peak intensity at two different temperatures. The symbols are explained in the legend.

16*e* sites. Indeed, this conclusion is also corroborated by the observation that the ν_2 and ν_4 Raman peaks of the ammonium ion in NH_4NbWO_6—around 1671 and 1410 cm^{-1}, respectively —are very broad, with a FWHM greater than 30 cm^{-1} (36). Keeping the ammonium ions fixed at the special positions 4*b* and 4*d*—$F\bar{4}3m$—yielded a nitrogen isotropic displacement parameter of 8.7(5) $Å^2$, which compares well with the value of 8.8(2) $Å^2$ given by Kuntz *et al.* (20).

The refinement using W/Nb anisotropic displacement parameters converges in such a way that the resulting matrix of displacement coefficients has one small but negative eigenvalue. This nonphysical value could result from a particular arrangement of W/Nb cations in the B_2O_6 sublattice, as commonly found in ABO_3 perovskites in which the *B* site is occupied by cations of different size and charge (39).

In the X-ray powder diffraction pattern of NH_4NbWO_6, there is also evidence that a kind of short-range ordering could be affecting the width and intensity of several weak peaks. This can be seen in Fig. 8, where the FWHM of several individually fitted Bragg peaks is plotted as a function of the diffraction angle. From the magnitude of the broadening of certain reflections and with the assumption that this effect is due solely to size broadening (40), the typical domain size was estimated to be 200 Å. This ordering could result from the ability of the ammonium ion in establishing hydrogen bonds with the oxygen atoms from the framework (20). Indeed, from Fig. 8 we can observe that no anisotropic broadening occurs with the related defect pyrochlore $RbNbWO_6$. Several attempts to model this structural disorder in the ammonium network in terms of a variable occupation factor of the two 16*e* sites were unsuccessful. The ordering of the ammonium network could also

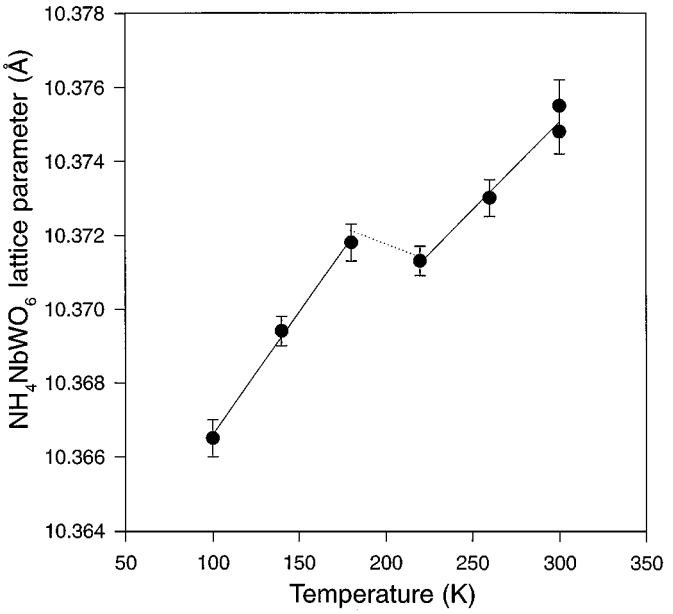

FIG. 4. Temperature dependence of the ammonium tungstoniobate lattice parameter, showing a slight discontinuity below 220 K. This transition is accompanied by an increase in the average thermal expansion coefficient in going from ambient ($F\bar{4}3m$) to the low-temperature phase. The structure below 220 K remains cubic (possibly $F23$). The line is just a guide for the eyes.

affect the W/Nb position inside the oxygen octahedra. This will be manifested in the structural model mainly through the W/Nb anisotropic displacement parameters, thus increasing the intensity of the 420 and other small Bragg peaks observed in the diffraction pattern.

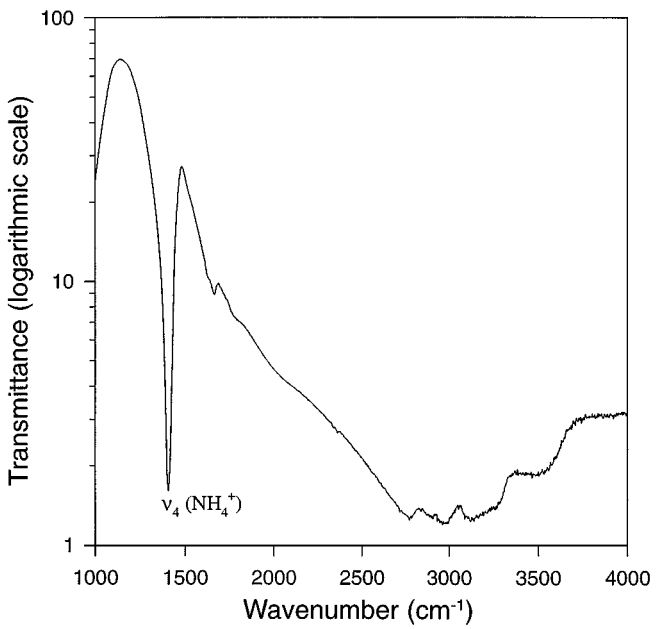

FIG. 5. Infrared transmittance spectrum of NH_4NbWO_6 dispersed in a KBr disk, showing the water bands at 1660 and 3530 cm^{-1}. The small features at about 3000 cm^{-1} are bands due to normal vibrations and overtones of the ammonium ion.

TABLE 1
Details of the Rietveld Refinement of the NH_4NbWO_6 Room Temperature X-Ray Powder Diffraction Pattern

2θ range (deg)	13.02–125.00
Step size (deg)	0.02
Counting time per step (s)	20
Zero-point error (deg)	− 0.0255(4)
Crystal symmetry	Cubic
Space group, Z	$F\bar{4}3m$, 8
Cell parameter a (Å)	10.3755(6)
Formula weight (g/mol)	390.77
Calculated density ρ (g/cm^3)	4.65
Half-width parameters (deg)	
U	0.1362(9)
V	− 0.005(2)
W	0.0222(2)
Number of reflections	138
Number of refined parameters	21
Profile R factors[a] (%)	
R_p	5.2
R_{wp}	7.3
χ^2	4.3

[a] Profile reliability factors were calculated according to $R_p = 100\sum|y_i(\text{obs}) - y_i(\text{calc})|/\sum|y_i(\text{obs})|$ and $R_{wp} = 100\{(\sum w_i[y_i(\text{obs}) - y_i(\text{calc})]^2)/\sum w_i[y_i(\text{obs})]^2\}^{1/2}$, where $w_i = 1/y_i(\text{obs})$.

The acentric symmetry of some defect pyrochlores already has been reported by Sleight *et al.* (43), who concluded that the actual crystal structure of AB_2O_6 defect pyrochlores is, in general, more complicated than the commonly assigned cubic $Fd\bar{3}m$ symmetry. The choice of a model structure for NH_4NbWO_6 based in space group $F\bar{4}3m$ is also consistent with other studies of defect pyrochlores in which partial oxygen ordering leads to the loss of inversion symmetry and, consequently, a reduction from $Fd\bar{3}m$ symmetry (44–46). For ammonium tungstoniobate, according to the results in Table 2, the cations W/Nb in the $F\bar{4}3m$

TABLE 2
Site Symmetries, Refined Atomic Positions, and Displacement Parameters Obtained from the Rietveld Refinement of Ammonium Tungstoniobate

Atom	Site	Occupation[a]	x	y	z	B (Å^2)
Nb	16e	0.5	0.1290(1)	0.1290(1)	0.1290(1)	1.7[b]
W	16e	0.5	0.1290(1)	0.1290(1)	0.1290(1)	1.7[b]
N(1)	16e	0.25	0.511(2)	0.511(2)	0.511(2)	1.1(4)
N(2)	16e	0.25	0.797(2)	0.797(2)	0.797(2)	1.1(4)
O(1)	24f	1.0	0.184(1)	0	0	1.4(1)
O(2)	24g	1.0	0.445(1)	1/4	1/4	1.4(1)

[a] Not refined.

[b] Equivalent isotropic displacement parameter obtained from $\beta_{11} = \beta_{22} = \beta_{33} = 0.0040(1)$; $\beta_{12} = \beta_{13} = \beta_{23} = -0.0028(1)$.

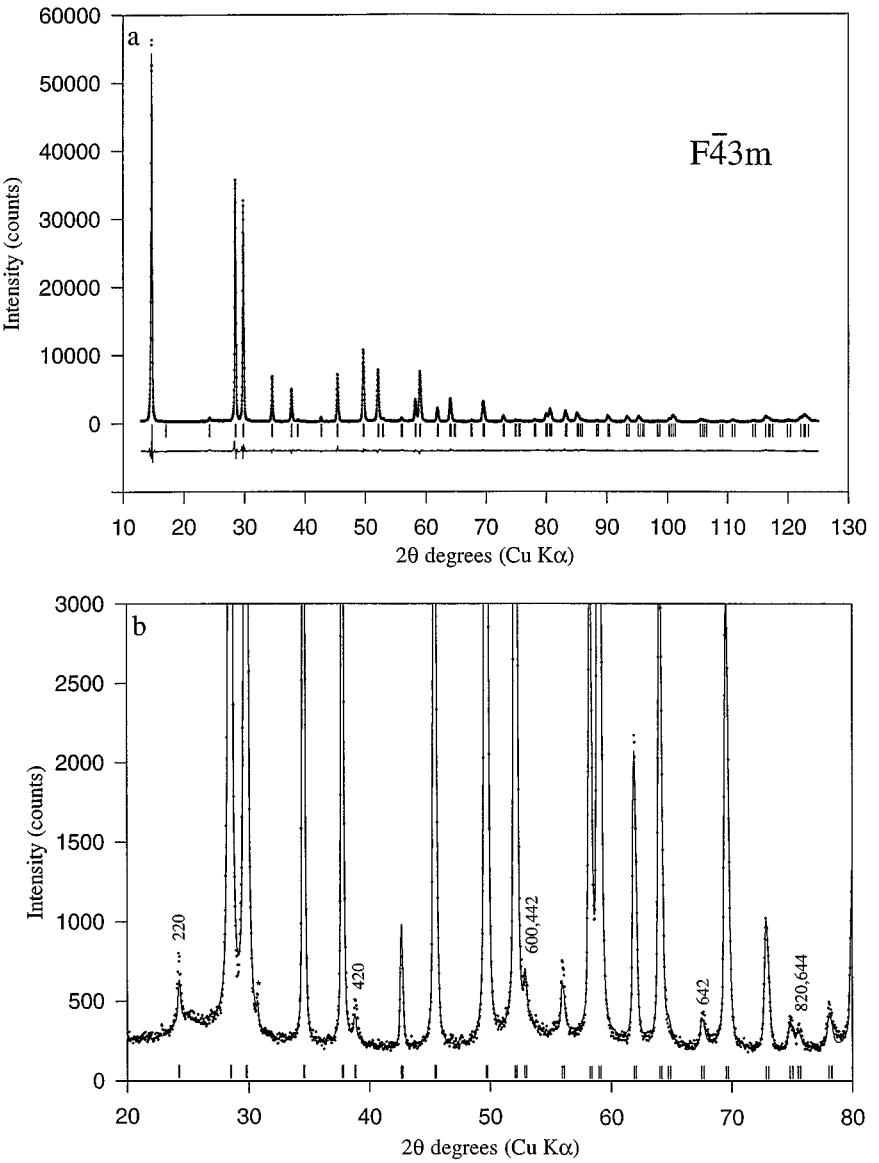

FIG. 6. (a) Rietveld refined profile of NH_4NbWO_6 under ambient conditions using the space group $F\bar{4}3m$. Dots indicate the raw data points and the solid line is the refined profile. Plotted on the same scale below is the difference between the observed and calculated profiles. Tick marks indicate the calculated positions of all permitted reflections in $F\bar{4}3m$. (b) Expanded view of (a) giving the correct indexation of the weak peaks. The asterisk marks the most intense peak of $RbCO_3$.

structure are slightly shifted by about 0.072 Å from the center of the oxygen octahedra along the [111] direction. It is already known that, in general, the magnitude of this out-of-center distortion is influenced, among other things, by the valence and size of the octahedrally coordinated cation (47).

Off-center cation displacement associated with some kind of oxygen–vacancy ordering was the mechanism proposed to explain the observation of $Fd\bar{3}m$-forbidden weak lines in some $A_2B_2O_{7-x}$ defect pyrochlores (45, 46, 48). It is noteworthy that such oxygen–vacancy ordering is observed in defect pyrochlores in which the large cation A is highly polarizable (Pb^{2+}, Tl^{+}, and Bi^{3+}, for example) and thus, it appears that the polarizability of the large cation A plays a key role in the mechanism responsible for the off-center cation displacement in defect pyrochlores $A_2B_2O_{7-x}$ (44, 48). In particular, for the defect pyrochlore NH_4NbWO_6, the presence of hydrogen bonds between the ammonium ions and the nearest oxygen in the B_2O_6 framework (20) can be related with off-center cation displacement and possibly could account for the transition from $Fd\bar{3}m$ to $F\bar{4}3m$.

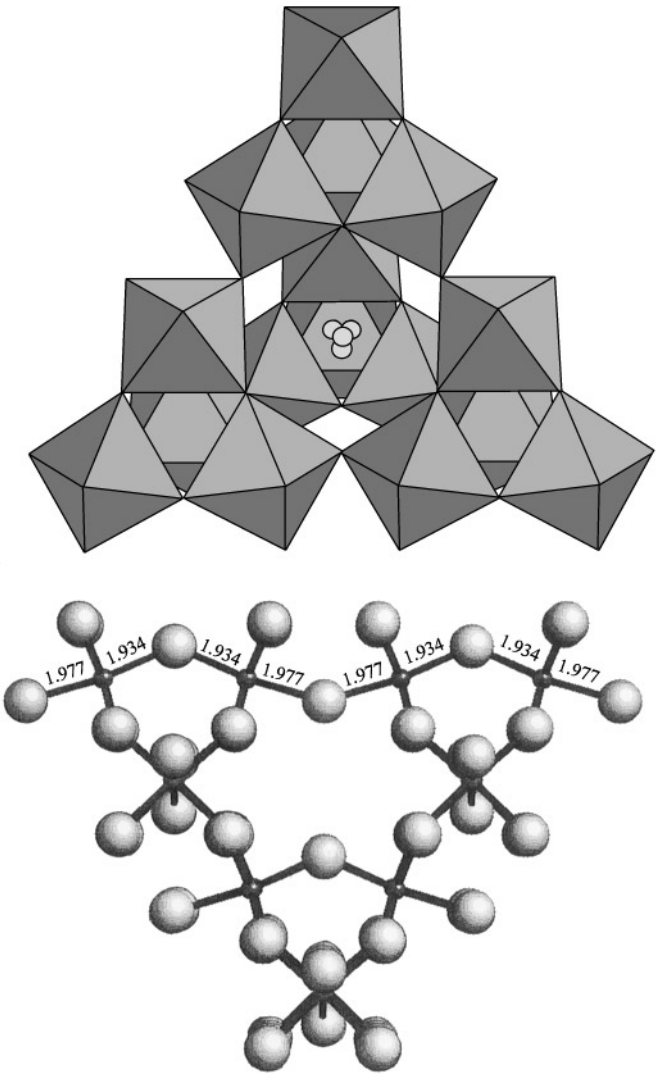

FIG. 7. Top: Refined crystal structure of NH_4NbWO_6, space group $F\bar{4}3m$. The B_2O_6 framework is composed of corner-shared oxygen octahedra with W/Nb cations (not shown in this figure) positioned near the center of each octahedron. The ammonium ion is represented as small spheres near the center of the cavity. Only one-quarter of the 16*e* equivalent positions are actually occupied by nitrogen ions. Bottom: Detail of the B_2O_6 network, showing the particular arrangement of W/Nb cations (small spheres) octahedrally coordinated by oxygen (large spheres). Distances W/Nb–O are quoted in angstroms.

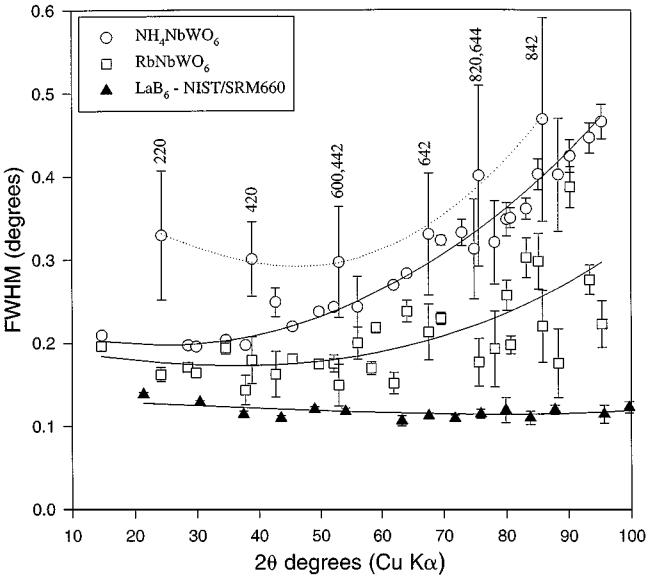

FIG. 8. Angular dependence of the FWHM for several individually fitted Bragg peaks from the X-ray diffraction patterns of NH_4NbWO_6, $RbNbWO_6$, and LaB_6 standard (27). The Miller indices of some ammonium tungstoniobate broadened peaks are displayed. Solid and dotted lines are the resulting fitting for the angular dependency of the FWHM (41). Peaks were individually fitted to a pseudo-Voigt profile function using the program XFIT (42), taking into account the Cu$K\alpha_1$ and Cu$K\alpha_2$ contributions. Symbols are identified in the box at the upper left corner of the figure.

CONCLUSION

In this work the crystal structure of ammonium tungstoniobate under ambient conditions has been revised. The results obtained indicate that the actual symmetry of this defect pyrochlore is better described by the noncentrosymmetric $F\bar{4}3m$ space group instead of the commonly assigned $Fd\bar{3}m$ space group. This conclusion is supported by the unequivocal presence of an $Fd\bar{3}m$-forbidden 420 reflection in the diffraction pattern at room temperature as well as by its continuous and reversible intensity decrease with temperature up to 533 K. This particular behavior suggests the onset of a second-order phase transition and consequently a group–subgroup relationship between the symmetry groups of the low- and high-temperature phases. The analysis of the temperature dependence of the integrated intensity of the Bragg peak 420 yielded a value of 455 ± 11 K for the transition temperature from the phase with $F\bar{4}3m$ symmetry to the high-temperature $Fd\bar{3}m$ phase.

The picture that emerges from the Rietveld analysis of the NH_4NbWO_6 X-ray diffraction pattern is consistent with the results obtained from vibrational spectroscopy experiments as well as from early studies on other defect pyrochlores. Further studies will be necessary to better understand the actual mechanism behind the cation ordering and its role in the high-temperature phase transition described in this paper.

ACKNOWLEDGMENTS

This work was partially financed by CNPq, FAPERGS, and FINEP (Brazil). The authors thank Dr. P. Brenner (IQ/UFRGS) for thermal gravimetric analysis, Dr. T. M. H. Costa for help with the vacuum cell for high-temperature FTIR spectroscopy, and Dr. M. A. Z. Vasconcellos for the electron microprobe analysis. O. J. Machado, M. G. Wieliczko, and Dr. R. Hinrichs, who provided the samples of $RbNbWO_6$ and NH_4NbWO_6 used in this work, are also gratefully acknowledged.

REFERENCES

1. A. F. Wells, *in* "Structural Inorganic Chemistry," 2nd ed., p. 502. Oxford Univ. Press, Oxford, 1950.
2. W. R. Cook, Jr., and H. Jaffe, *Phys. Rev.* **88,** 1426 (1952).
3. V. I. Voronkova, A. A. Bosenko, and V. K. Yanovskii, *Sov. Tech. Phys. Lett.* **12,** 402 (1987).
4. M. Hervieu, C. Michel, and B. Raveau, *Bull. Soc. Chim. Fr.* **11,** 3939 (1971).
5. D. Babel, G. Pausewang, and W. Viebahn, *Z. Naturforsch. B* **22,** 1219 (1967).
6. F. J. Rotella, J. D. Jorgensen, B. Morosin, and R. M. Biefeld, *Solid State Ionics* **5,** 455 (1981).
7. M. A. Butler and R. M. Biefeld, *Solid State Commun.* **29,** 5 (1979).
8. M. Catti, C. M. Mari, E. Cazzanelli, and G. Mariotto, *Solid State Ionics* **40/41,** 900 (1990).
9. S. V. Bhat, N. Binesh, and V. Bhat, *Chem. Phys. Lett.* **231,** 487 (1994).
10. N. Ruchaud, J. Grannec, A. Tressaud, and P. Gravereau, *C. R. Acad. Sci., Ser. 2B* **321,** 507 (1995).
11. J. L. Fourquet, C. Jacoboni, and R. de Pape, *Mater. Res. Bull.* **8,** 393 (1973).
12. M. Kuntz and G. Tomandl, *Solid State Ionics* **25,** 121 (1987).
13. A. V. Powell and P. G. Dickens, *Appl. Phys. A* **51,** 226 (1990).
14. T. S. Chernaya, N. N. Bydanov, L. A. Muradyan, V. A. Sarin, and V. I. Simonov, *Sov. Phys. Crystallogr.* **33,** 40 (1988).
15. B. Chakoumakos, J. *Solid State Chem.* **53,** 120 (1984).
16. W. W. Barker, J. Graham, O. Knop, and F. Brisse, *in* "The Chemistry of Extended Defects in Non-metallic Solids" (L. Eyring and M. O'Keefe, eds.), p. 198. North-Holland, Amsterdam, 1970.
17. B. Darriet, M. Rat, J. Galy, and P. Hagenmuller, *Mater. Res. Bull.* **6,** 1305 (1971).
18. D. Groult, C. Michel, and B. Raveau, *J. Inorg. Nucl. Chem.* **36,** 61 (1974).
19. D. G. Brunner and G. Tomandl, *Adv. Ceram. Mater.* **2,** 794 (1987).
20. M. Kuntz, G. Tomandl, and A. Hoser, *Solid State Ionics* **27,** 211 (1988).
21. H. Möller, W. Müller-Warmuth, M. Kuntz, and G. Tomandl, *Ber. Bunsenges. Phys. Chem.* **93,** 140 (1989).
22. R. Hinrichs, G. Tomandl, and J. A. H. da Jornada, *Solid State Ionics* **77,** 257 (1995).
23. C. A. Perottoni and J. A. H. da Jornada, *Phys. Rev. Lett.* **78,** 2991 (1997).
24. J. Rodríguez-Carvajal, *in* Abstracts, Satellite Meeting on Powder Diffraction, XVth Conference of the International Union of Crystallography, Toulouse, France, p. 127, 1990.
25. L. W. Finger, D. E. Cox, and A. P. Jephcoat, *J. Appl. Crystallogr.* **27,** 892 (1994).
26. M. A. G. Aranda, E. R. Losilla, A. Cabeza, and S. Bruque, *J. Appl. Crystallogr.* **31,** 16 (1998).
27. T. G. Fawcett, C. E. Crowder, S. J. Brownell, *et al.*, *Powder Diffr.* **3,** 209 (1988).
28. T. M. H. Costa, M. R. Gallas, E. V. Benvenutti, and J. A. H. da Jornada, *J. Non-Cryst. Solids* **220,** 195 (1997).
29. L. Landau and E. Lifshitz, "Physique Statistique." Mir, Moscow, 1967.
30. O. V. Kovalev, *Sov. Phys. Solid State* **2,** 1105 (1960).
31. E. K. H. Salje, "Phase Transitions in Ferroelastic and Co-elastic Crystals." Cambridge Univ. Press, Cambridge, UK, 1993.
32. H. E. Stanley, "Introduction to Phase Transitions and Critical Phenomena." Clarendon, Oxford, 1971.
33. A. V. Astaf'ev, A. A. Bosenko, V. I. Voronkova, M. A. Krasheninnikova, S. Yu. Stefanovich, and V. K. Yanovskii, *Sov. Phys. Crystallogr.* **31,** 575 (1986).
34. N. N. Bydanov, T. S. Chernaya, L. A. Muradyan, V. A. Sarin, E. É. Rider, V. K. Yanovskii, and A. A. Bosenko, *Sov. Phys. Crystallogr.* **32,** 363 (1987).
35. D. W. Murphy, R. J. Cava, K. Rhyne, R. S. Roth, A. Santoro, S. M. Zahurak, and J. L. Dye, *Solid State Ionics* **18&19,** 799 (1986).
36. C. A. Perottoni and J. A. H. da Jornada, to be published.
37. F. Bertaut, *J. Phys. Radium* **13,** 499 (1952).
38. D. E. Williams, *Acta Crystallogr., Sect. A* **27,** 452 (1971).
39. T. Sekiya, T. Yamamoto, and Y. Torii, *Bull. Chem. Soc. Jpn.* **57,** 1859 (1984).
40. R. Delhez, T. H. de Keijser, J. I. Langford, D. Louër, E. J. Mittemeijer, and E. J. Sonneveld, *in* "The Rietveld Method" (R. A. Young, ed.), p. 132. Oxford Univ. Press, New York, 1996.
41. G. Caglioti, A. Paoletti, and F. P. Ricci, *Nucl. Instrum. Methods* **35,** 223 (1958).
42. A. A. Coelho and R. W. Cheary, Collaborative Computational Project, CCP14, 1996 (http://gserv1.dl.ac.uk/CCP/CCP14/index.html).
43. A. W. Sleight, F. C. Zumsteg, J. R. Barkley, and J. E. Gulley, *Mater. Res. Bull.* **13,** 1247 (1978).
44. V. Kahlenberg and H. Böhm, *J. Alloys Compd.* **223,** 142 (1995).
45. J. A. Alonso, C. Cascales, I. Rasines, and J. Pannetier, *Physica B* **156&157,** 107 (1989).
46. B. J. Kennedy, *J. Solid State Chem.* **123,** 14 (1996).
47. M. Kunz and I. D. Brown, *J. Solid State Chem.* **115,** 395 (1995).
48. R. A. Beyerlein, H. S. Horowitz, J. M. Longo, M. E. Leonowicz, J. D. Jorgensen, and F. J. Rotella, *J. Solid State Chem.* **51,** 253 (1984).